Clumped isotopologue fractionation by microbial cultures performing the anaerobic oxidation of methane

Shuhei Ono[1,*], Jeemin H. Rhim[1], Danielle S. Gruen[1,†], Heidi Taubner[2], Martin Kölling[2], Gunter Wegener[2,3]

[1] *Department of Earth, Atmospheric and Planetary Science, Massachusetts Institute of Technology, Cambridge, MA USA.* sono@mit.edu, jrhim@mit.edu, dgruen@alum.mit.edu

[2] *MARUM Center for Marine Environmental Science, University of Bremen, Bremen, Germany.*

[3] *Max Planck Institute for Marine Microbiology, Bremen, Germany.* gwegener@mpi-bremen.de

A manuscript prepared for submission to *Geochimica Cosmochimica Acta*

*corresponding author, sono@mit.edu

†: present address, Department of Surgery, University of Pittsburgh, Pittsburgh, PA 15213

Abstract

Methane is abundant in marine subsurface sediments, sourced from microbial or thermocatalytic products. The relative composition of its isotopologues ($^{12}CH_4$, $^{13}CH_4$, $^{12}CH_3D$ and $^{13}CH_3D$) is used to infer its sources and sinks. The anaerobic oxidation of methane (AOM) is an important methane sink reaction carried out by consortia of anaerobic methanotrophic archaea (ANME) and partner bacteria in the presence of methane and sulfate. We investigated the methane isotopologue fractionations during AOM in experiments with cultures of ANME-1 archaea and partner bacteria obtained from hydrothermally heated gas-rich sediments of the Guaymas Basin. During partial methane consumption in four sets of experiments, residual methane became enriched in $^{13}CH_4$ and $^{12}CH_3D$, following kinetic fractionations from 11.1 to 18.3 ‰ and from 117 to 180 ‰, respectively. Results from one set of experiments with D-depleted medium water ($\delta D = -200$‰, whereas the control was –55‰) suggest the potential reversibility during methane activation step, which would contributes to equilibrium as opposed to kinetic fractionations. The value of $\Delta^{13}CH_3D$ (the abundance of $^{13}CH_3D$ with respect to that expected from stochastic distribution) increased toward and beyond (up to 8.4‰) the value expected for isotopologue equilibrium (5.3‰ at 37 °C). The kinetic clumped isotopologue fractionation (difference between $^{13}CH_3D/^{12}CH_3D$ and $^{13}CH_4/^{12}CH_4$ fractionations) of 4.8 to 12.8 ‰ is in contrast with our previous observation of little to no clumped isotopologue effect during aerobic methane oxidation. Our results demonstrate that AOM can contribute to near-equilibrium $\Delta^{13}CH_3D$ values observed in marine sediments and $^{13}CH_3D$ systematics can be used to distinguish aerobic versus anaerobic methanotrophic processes in nature.

1 Introduction

Marine sediments store about 500 to 5000 Gt of methane (Milkov 2004; Buffett and Archer, 2004). This methane derives from three main sources. In deep marine sediments, typically a few km or deeper, thermogenic methane is produced via the thermocatalytic decay of organic matter (e.g., Tissot et al., 1974). In shallower anoxic sediments and petroleum reservoirs, typically below ca. 60 to 80 °C, archaea produce methane as a metabolic product (Reeburgh, 2007; Inagaki et al., 2015; Wilhelms, 2001). A minor component of marine methane may originate from abiotic methane production during the alteration of seafloor rocks (e.g., Klein et al., 2019; McDermott et al., 2015; Wang et al., 2018). The origins of methane are often inferred based on its carbon ($^{13}C/^{12}C$) and hydrogen (D/H) isotopic compositions (e.g., Schoell, 1980; Whiticar, 1999). Methane that is depleted in ^{13}C by < –45‰ (with respect to PDB) is usually interpreted as microbial in origin. Thermogenic methane is usually more ^{13}C-enriched. The boundaries between these values are not well defined.

In addition to bulk isotope ratios, the relative abundance of rare methane isotopologues with multiple heavy isotope substitutions (e.g., $^{13}CH_3D$ and $^{12}CH_2D_2$), also known as clumped isotopologues, has been proposed as a tool to gauge the temperature of methane generation or isotopic re-equilibration (Stolper et al., 2014a,b; Wang et al., 2015; Young et al., 2017). This approach is based on the isotopologue exchange reaction:

$$^{13}CH_4 + {}^{12}CH_3D \leftrightarrow {}^{13}CH_3D + {}^{12}CH_4. \quad (1)$$

The equilibrium constant of this reaction primarily depends on temperature, approaching unity at high temperatures (1.0002 at 1,000 °C) and expected to be about 1.0057 at 25 °C. The effects of pressure, hydration, salinity etc. are expected to be small but have not been carefully examined. Thus, precise measurements of four isotopologues of methane yield the apparent temperature that is expected if isotopologues were thermally equilibrated. Studies thus far have shown that the clumped isotopologue composition of methane from subsurface environments (e.g., marine sediment pore water, natural gas deposits) often yields reasonable formation temperatures, whereas methane sampled from surface environments (e.g., ruminants, lakes, and swamps) is characterized by clear kinetic signals that yield apparent clumped isotopologue temperatures much higher than the

environmental temperatures (Ash et al., 2019, Douglas et al., 2017, 2020; Giunta et al., 2019; Stolper et al., 2014b, 2015; Wang et al., 2015; Young et al., 2017).

The kinetic isotopologue signals from surface methane are consistent with those from laboratory culture experiments, in which methanogens consistently produced methane with non-equilibrium isotopologue compositions (Wang et al., 2015; Douglas et al., 2017 2020; Young et. al., 2017; Gruen et al., 2018; Stolper et al., 2015). Previous studies have also investigated the clumped methane isotopologue fractionation during sink reactions, including aerobic methane oxidation (Wang et al., 2016) and gas phase methane oxidation by OH and Cl radicals (Whitehill et al., 2017; Joelsson et al., 2014, 2016). Both processes fractionate isotopologues in such a way that the remaining methane is more depleted in $^{13}CH_3D$, which brings $^{13}CH_3D$ abundance away from that expected for equilibrium. Therefore, questions remain as to how methane with apparent equilibrium isotopologue signals can be produced in marine subsurface environments. It has been hypothesized that methane with equilibrium isotopologue composition is linked to high reversibility of slow methanogenesis in low-energy environments (Stolper et al., 2015; Wang et al., 2015; Okumura et al., 2016) and/or the result of the anaerobic oxidation of methane (AOM) (Ash et al., 2019; Giunta et al., 2019; Okumura et al., 2016). A question remains whether AOM is *required* to produce equilibrium δD and $\Delta^{13}CH_3D$ (and $\Delta^{12}CH_2D_2$) signals. We note that similar questions were raised for sulfur isotope systems whether near-equilibrium $^{34}S/^{32}S$ fractionation requires oxidative sulfur cycles or can be produced by microbial sulfate reduction alone (e.g., Canfield and Thamdrup, 1994; Sim et al. 2011).

The AOM is performed by anaerobic, methane-oxidizing archaea (ANME) that form consortia with sulfate-reducing bacteria (reviewed in Knittel et al., 2019). The ANME are relatives of methanogens and they reverse the entire methanogenesis pathway for methane oxidation (Hallam et al., 2004; Meyerdierks et al., 2010). The effect of AOM on carbon and hydrogen isotopic compositions of methane has been investigated in multiple studies. At seawater sulfate concentrations (28 mM), AOM has kinetic carbon and hydrogen isotope fractionations resulting in the enrichment of ^{13}C and D in the remaining methane (Holler et al., 2009). In contrast, AOM at low sulfate concentrations results in ^{13}C-depletion in the remaining methane. The decreasing methane carbon isotopic compositions

were explained as isotopic equilibration between methane and inorganic carbon mediated by AOM (Yoshinaga et al., 2014). The different availability of sulfate may explain the variant methane isotope patterns observed in AOM active marine sediments (Borowski et al., 1997; Pohlman et al., 2008; Yoshinaga et al., 2014). Similar studies for the hydrogen isotope systematics have not been published.

This study experimentally examines the bulk ($^{13}C/^{12}C$ and D/H) and clumped isotopologue ($^{13}CH_3D$) fractionation of AOM. The cultures used in this study consist of consortia of ANME of the ANME-1 clade and the partner bacteria of the Seep-SRB2 group (Holler et al., 2011a; Krukenberg et al., 2018). To reveal the isotope fractionation patterns of AOM, we measured the relative abundance of four isotopologues, $^{12}CH_4$, $^{13}CH_4$, $^{12}CH_3D$ and $^{13}CH_3D$ of methane remaining in the cultures. The fractionation of $^{13}CH_3D$ for AOM is characteristically different from that of aerobic methane oxidation reported in a previous study (Wang et al., 2016). Our study suggests that AOM may contribute to, although is not necessarily required for, the near-equilibrium isotopologue signals observed in marine environments.

2 Methods

2.1 Description of culture experiments

All experiments were performed with sediment-free 37 °C AOM enrichment cultures obtained from hydrothermally-heated, gas-rich sediments of the Guaymas Basin sampled during RV Atlantis cruise AT15-56 with the submarine ALVIN in December 2009. The cultivation procedures, physiological properties and microbial compositions of this culture have been described before (Laso-Pérez et al., 2018; Holler et al., 2011a; Krukenberg et al., 2018; Wegener et al., 2016).

The analysis of methane clumped isotopologue composition requires a relatively large gas sample of 40 µmol or more methane. To meet this requirement, we performed four different (C, B, D and N) series of 6 to 11 replicate incubations each (Table 1). Experiment C- and B-series were run as duplicates (the same starting methane and carried out at the same time). D- and N- series used the same starting methane but D-series used D-depleted water medium (δD_{H2O} = –200‰, Table 1) to test the potential exchange of H

147 isotopes between water and methane. N-series (normal D-experiment, $\delta D_{H2O} = -55‰$) is a
148 control for D-series that was run simultaneously with the D-series. Experiment X-series
149 are the abiotic control experiments run at the same time as B- and C-series experiments.
150 These control experiments were not inoculated in order to test the potential isotopologue
151 fractionation during sample processing.
152 For the experiment, a suitable amount of culture targeting a methane-dependent
153 sulfate reduction rate of 100 to 150 μmol l^{-1} d^{-1} was homogenized by stirring in an anoxic
154 chamber free of hydrogen gas. The homogenized culture was supplied with fresh artificial
155 saline medium with seawater sulfate concentration (28 mM) and 10 mM dissolved
156 inorganic carbon (DIC). The culture was then equally distributed to 70-ml culture vials and
157 filled up completely with culture medium. For the experiment with low D-H_2O (D-series),
158 the culture medium was prepared with 200 ml D-depleted water (≤ 1ppm D, Sigma-
159 Aldrich) and 800 ml ultrapure water.
160 The completely filled and closed culture bottles were removed from the chamber and
161 7 ml of the medium volume was replaced with 20 ml of methane:CO_2 (90:10) gas mixture
162 that supplied 0.75 mmol methane to the culture. Hence, all experiments were performed
163 under excess of sulfate (1.76 mmol per vial). All bottles were transferred into a 37 °C
164 incubator equipped with a shaking table operated at 70 rpm. Due to constant agitation of
165 the bottles and the slow AOM rate, all reactants and products of AOM including methane
166 isotopologues are considered to be equilibrated between liquid and headspace. Sulfide
167 concentrations for samples were measured every 3 to 5 days from 0.1 ml sample volume
168 in a miniaturized 4 ml copper sulfate assay (Cord-Ruwish, 1985). The increase of sulfide
169 concentrations was used to determine the amount of methane consumed in the samples,
170 assuming 1:1 stoichiometry between methane oxidation and sulfide production, according
171 to the reaction stoichiometry, $CH_4 + SO_4^{2-} \rightarrow HCO_3^- + HS^- + H_2O$.
172 At the beginning of the experiment and when reaching designated sulfide
173 concentrations (i.e., reaching specific partial methane consumption values), these bottles
174 were sampled for different measurements. The liquid phase was sampled for the
175 measurement of DIC isotopic compositions (filtration of 6 ml medium into Exetainer®
176 vials, Labco) and the determination of hydrogen isotopic composition of water (filtration
177 of 2 ml into Exetainer). Then, the culture headspace was completely replaced with anoxic

DIC-free medium, while a syringe concurrently collected the headspace (methane). This gas was transferred to another culture vial that was filled with 10 % NaOH solution by displacement.

2.2 Isotope ratio analyses

Isotope ratios are reported using standard delta-notation:

$$\delta^{i}\mathrm{A} = \frac{\left({}^{i}\mathrm{A}/{}^{j}\mathrm{A}\right)_{sample}}{\left({}^{i}\mathrm{A}/{}^{j}\mathrm{A}\right)_{reference}} - 1 \quad (2)$$

Where, ^{i}A is ^{2}H (symbol D is used as deuterium), ^{13}C, or ^{18}O, for the isotope ratio ($^{i}A/^{j}A$), $^{2}H/^{1}H$, $^{13}C/^{12}C$ or $^{18}O/^{16}O$, respectively. Following IUPAC recommendations, the commonly used multiplication factor of 1000 is omitted from the definition since it technically belongs to per mil (‰) (Coplen, 2011).

Hydrogen isotopic compositions of medium water (δD_{H2O}) were measured by cavity ring-down spectrometry (Picarro L-2130-i). The geometric mean and relative standard deviations are calculated from the last three of nine 7 µl injections of a 0.2 µm-filtered water sample. The results are calibrated against the VSMOW2 and SLAP2 isotope standards. For calibration, we used 39:1, 19:1, 9:1 and 5:1 mixtures of our lab standard "LMOW" ($\delta^{18}O$ = +0.10‰, δD = +0.45‰ on the VSMOW2-SLAP2 scale) and SLAP2.

Carbon isotopic compositions of DIC were determined by isotope ratio infrared spectrometry (IRIS; Thermo Scientific Delta Ray IRIS with URI connect and Cetac ASX-7100 Autosampler). Measurement vials (12 ml Exetainer® vials; Labco) were filled with 100 µl phosphoric acid (45%) and headspace was flushed and replaced with synthetic air for 3 minutes. Samples (1 ml each) were injected via a syringe and kept at room temperature for transformation of DIC into CO_2. After 10 hours of equilibration, the carbon isotopic composition of CO_2 of each sample was analyzed.

2.3 Methane isotopologue analysis

Samples of methane (>40 µmol) were purified by cryogenic distillation to remove water and CO_2, followed by cryofocusing-preparative gas chromatography (Wang et al., 2015; Wang et al., 2016). Preparative gas chromatography is equipped with a packed

column (Carboxen-1000, 5'×1/8", Supelco) held at 30 °C with helium carrier gas. The eluted methane was trapped on activated charcoal at liquid nitrogen temperature. The relative abundances of $^{12}CH_4$, $^{13}CH_4$, $^{12}CH_3D$ and $^{13}CH_3D$ were measured using tunable infrared laser direct absorption spectroscopy (TILDAS) described previously by Ono et al. (2014).

Results in Table 1 show 95% confidence interval for the spectroscopic measurements, typically 0.2 to 0.4 ‰ for $\Delta^{13}CH_3D$ values. This does not include potential fractionation during sample preparation. Data for abiotic control experiments (X-series, Table 1) show that the errors for sample preparation processes are comparable to the 95% confidence above. Most samples were measured by the recycle mode, in which sample CH_4 was recovered from the TILDAS absorption cell to the cold trap, and reintroduced to TILDAS for 6 to 10 times. This allows repeated comparison of sample against reference gas. Thus, precision is not necessarily a function of sample size. Isotope values are reported using standard delta notation against PDB and SMOW for the ratios $^{13}C/^{12}C$ and D/H, respectively. This isotope scale was calibrated by the measurements of NGS-1 and NGS-3 (Wang et al., 2016).

We define $\Delta^{13}CH_3D$ value as a measure of the abundance of $^{13}CH_3D$ relative to stochastic distributions (Ono et al., 2014):

$$\Delta^{13}\mathrm{CH_3D} = \ln\left(\frac{^{13}\mathrm{CH_3D}}{^{12}\mathrm{CH_3D}} \cdot \frac{^{12}\mathrm{CH_4}}{^{13}\mathrm{CH_4}}\right) \quad (3)$$

The relationship between $\Delta^{13}CH_3D$ values and apparent methane generation temperatures is based on the formula

$$\Delta^{13}\mathrm{CH_3D(T)} = -0.11006\left(\frac{1000}{T}\right)^3 + 1.04151\left(\frac{1000}{T}\right)^2 - 0.55235\left(\frac{1000}{T}\right) \quad (4)$$

where T is temperature in Kelvin. The equation is approximated from the solution based on the fundamental vibrational frequencies calculated by density functional theory (Whitehill et al., 2017). Equation (4) produces lower $\Delta^{13}CH_3D$ values by 0.1±0.01‰ (for the temperature range from 20 to 160 °C) compared to the recent calibration by Eldridge et al. (2019).

2.4 Calculation of isotope fractionation factors

Isotope fractionation factors (α values) are calculated based on the conventional Rayleigh equation (Mariotti et al., 1981):

$$\ln(\delta^{13}\mathrm{C}+1) = \ln(\delta^{13}\mathrm{C}_0+1) + (^{13}\alpha - 1)\cdot \ln f, \text{ and} \quad (5)$$

$$\ln(\delta\mathrm{D}+1) = \ln(\delta\mathrm{D}_0+1) + (^{2}\alpha - 1)\cdot \ln f. \quad (6)$$

Where f is the fraction of CH_4 remaining, and $^{13}\alpha$ and $^{2}\alpha$ are the kinetic isotope fractionation factors for carbon ($^{13}C/^{12}C$) and hydrogen (D/H) isotopes, respectively, and $\delta^{13}C_0$ and δD_0 are initial isotope compositions of methane. The kinetic fractionation factor is the ratio of the rate constants for $^{13}CH_4$ or $^{12}CH_3D$ relative to $^{12}CH_4$ (e.g., $^{13}\alpha = k_{13CH4}/k_{12CH4}$). The ε symbol is used to represent the departure of fractionation factors from unity ($^{13}\varepsilon = 1-^{13}\alpha$ or $^{2}\varepsilon = 1-^{2}\alpha$). Equations (5) and (6) are exact solutions when f is quantified as the fraction of $^{12}CH_4$ remaining (as opposed to total methane isotopologues). Fractionations (slopes) and their uncertainty are calculated by weighted least square method of York et al. (2004). Errors for H_2S concentrations are estimated to be 5% of measured value. For isotopologue ratios, 95% confidence interval for 4 to 8 measurements were used to estimate errors (Table 1; Figure 1).

The corresponding equation for the $\Delta^{13}CH_3D$ value is:

$$\Delta^{13}\mathrm{CH_3D} = \Delta^{13}\mathrm{CH_3D_0} + (^{13,2}\alpha - {}^{13}\alpha - {}^{2}\alpha + 1)\cdot \ln f \quad (7)$$

where, $^{13,2}\alpha$ is the isotopologue fractionation factor for $^{13}CH_3D$ relative to $^{12}CH_4$ (Wang et al., 2016). According to the rule of geometric mean (Bigeleisen, 1955), $^{13,2}\alpha$ is approximately equal to the product of $^{13}\alpha$ and $^{2}\alpha$ ($^{13,2}\alpha \simeq {}^{13}\alpha \cdot {}^{2}\alpha$). We define the deviation from the rule of geometric mean as the kinetic clumped isotopologue factor (γ):

$$^{13,2}\alpha = \gamma \cdot {}^{13}\alpha \cdot {}^{2}\alpha \quad (8)$$

For bond breaking processes, the reduction of the zero-point energy (ΔZPE) at transition state produces γ values less than unity (Whitehill et al., 2017) as discussed in section 3.2.

3 Results

Results of the experiments are reported in Table 1. Throughout the course of each experiment, AOM partially consumed methane, as indicated by increasing sulfide concentrations. The AOM consortia consumed 100 to 160 µmol of methane per liter per day, translating into about 0.9% to 1.6% of the supplied methane. The rates of AOM remained largely constant, due to the inherently slow growth of AOM communities with doubling times of about 90 days. After specific time intervals, single bottles were analyzed for headspace methane concentrations (*see* methods).

All four series of experiments showed kinetic isotope fractionations with progressive enrichment of the residual methane in isotopologues containing heavy (^{13}C and D) isotopes (Fig. 1). Fig. 1 illustrates the derived fractionations for the carbon isotope of 11.1‰ to 18.3‰ and hydrogen isotope fractionation of 117‰ to 180‰ (Fig. 1; Table 2). Experiments carried out at the same time and using the same starting culture (i.e., B- versus C-series, and N- versus D-series), yielded consistent fractionation factors, but the two sets of experiments yielded somewhat different fractionation factors. One reason for the different fractionation factors might be the slightly lower pH value in the later experiments (6.8 versus 7.2). This modification was introduced in between the two experiments to avoid carbonate precipitation in the cultures. Last two data points for D-series are not on the linear regression trend. Its implication to reversibility is discussed in section 4.1 and Appendix A. During the course of the experiments, the $\Delta^{13}CH_3D$ values of methane increased from 2.0±0.5‰ to up to 8.5‰, which is higher than the value expected for isotopologue equilibrium at experimental temperature ($\Delta^{13}CH_3D_{eq.}$ = 5.4‰ at 37 °C) (Table 1; Fig. 1).

4 Discussion

4.1 Kinetic isotopologue fractionations were observed during AOM

The observed ranges of kinetic fractionations for $^{13}C/^{12}C$ and D/H ratios (from 11.1‰ to 18.3‰ and from 117‰ to 180‰, respectively) are largely consistent with the previous study, where AOM cultures were adapted to and experimented at lower temperatures (12 and 20 °C) (Fig. 2; Holler et al., 2009).

283 In order to evaluate if the observed isotopologue effect is entirely kinetic, the
284 potential reversibility of AOM was investigated with cultures using media with different
285 δD compositions (D- and N-series, Table 1). The experiment with a strongly D-depleted
286 incubation medium (D-series, δD_{H2O} = –200‰) and an accompanying experiment with
287 medium without the D-depleted water (N-series, δD_{H2O} = –55‰) yielded inconclusive
288 results regarding the effect of δD values of medium water and the potential reversibility
289 for AOM. Although results of York regression (Figure 1e) yielded statistically different
290 D/H fractionations (116.5 ± 3.5 vs. 141.1 ± 6.0 for D- and N-series, respectively). The
291 shallower slope for D-series is largely due to the last two data points, where methane
292 consumption by AOM is above 50%. Because the normal δD_{H2O} experiments (N-series)
293 were not run above 47.5% methane consumption (Figure 1e, Table 1), the comparison of
294 D- and N-series remain inconclusive. During AOM, the δD values consistently increased
295 from the initial value of –190‰ up to –80‰ (Table 1). This is opposite from what is
296 expected for isotope equilibration between methane and water. It would drive methane δD
297 values lower towards equilibrium values, which are –360 and –244 ‰ for D- and N-series
298 experiments, respectively. Accurate evaluation of the degree of reversibility requires the
299 estimate of primary and secondary D/H fractionation factors. We present a preliminary
300 model in Appendix A, which suggests that reversibility could be as high as 60% during the
301 activation of methane with methyl-coenzyme M reductase (MCR) for experiments N- and
302 D-series, whereas the same model predict reversibility as much as 69% for B- and C-series)
303 (Fig. A2). Radiotracer (^{14}C) experiments with AOM cultures have demonstrated a
304 substantial amount (up to 5% of net AOM rate) of carbon back flux from the DIC to
305 methane (Holler et al., 2011b). Marlow et al. (2017) reported the rates of AOM estimated
306 from the production of $^{14}CO_2$ from $^{14}CH_4$ and HDO from $^{12}CH_3D$. They observed the rate
307 based on HDO production is a factor of two faster than that based on $^{14}CO_2$, suggesting the
308 back flux from MCR is 50% compared to the complete oxidation of CH_4 to CO_2 (Marlow
309 et al., 2017). If deuterium isotope effect is considered, the back flux would be higher than
310 50%, consistent with our estimate of 60% reversibility. Our focus is to present the data for
311 $^{13}CH_3D$ such that the detailed investigation of the reversibility is the scope for future
312 studies.

The values of $\Delta^{13}CH_3D$ of initial methane were 1.6‰ for C- and B-series, and 2.5‰ for D- and N-series. These values correspond to apparent clumped temperatures of 299 and 195 °C, respectively, suggesting a thermogenic origin. During the course of the experiments, the $\Delta^{13}CH_3D$ values of methane increased, and corresponding clumped temperature decreased towards experimental temperature of 37 °C, reaching an apparent isotopologue equilibration. For two experiments that consumed >70% of the supplied methane, however, $\Delta^{13}CH_3D$ values increased beyond that expected for equilibrium at 37 °C ($\Delta^{13}CH_3D_{eq.}$ = 5.4‰). The highest $\Delta^{13}CH_3D$ value of 8.5‰ (Table 2) translates to a clumped temperature of –46 °C. This is far below the incubation temperature of 37 °C and clearly indicates predominantly kinetic fractionation of the clumped isotopologue, $^{13}CH_3D$.

The increase of $\Delta^{13}CH_3D$ values of residual methane during oxidation is characteristic of AOM in our experiment. Fig. 3 compares the evolution of $\Delta^{13}CH_3D$ values observed during experiments for different methane oxidation processes. The value of $\Delta^{13}CH_3D$ for residual methane progressively decreased during methane oxidation by aerobic methanotrophic bacteria (*Methylococcus capsulatus*; Wang et al., 2016) as well as gas phase methane oxidations by OH and Cl radicals (Whitehill et al., 2017). Thus, although all three methane oxidation processes tested so far (AOM, aerobic methane oxidation, and gas phase oxidations) enriched the residual methane in ^{13}C and D-containing isotopologues, AOM yielded a distinguishable trend in terms of clumped isotopologue signals (Fig. 3). This could be attributed to the reaction mechanism intrinsic to methane activation by MCR, as discussed in the next section.

4.2 Transition state structure is linked to kinetic clumped isotopologue effects of AOM

Our experimental studies showed that methane oxidation by AOM increased the $\Delta^{13}CH_3D$ values of residual methane, in contrast to aerobic methanotrophy and gas phase oxidations, which decreased the $\Delta^{13}CH_3D$ values (Fig. 3). Following our definition of $\Delta^{13}CH_3D$ (Equation-3), the slopes in $-\ln(f)$ vs. $\Delta^{13}CH_3D$ plots (Fig. 1c and 1f) are determined by all three isotopologue fractionation factors ($^{13,2}\alpha$, $^{13}\alpha$ and $^{2}\alpha$; Equation-7). The calculated intrinsic clumped isotopologue fractionation factor (γ, Equation-8) for AOM ranges from 0.9872 to 0.9952 (Table 2). These γ values are much less than unity

compared to those measured for aerobic methanotrophy (1.0004±0.0006, Wang et al., 2016) and oxidation by OH and Cl radicals (0.9997±0.0012 and 0.9965±0.0007, respectively) (Whitehill et al., 2017). The different intrinsic γ values could be related to the transition state structure of the reaction and, thus, characteristic to the enzyme that catalyzes the reaction of aerobic vs. anaerobic methanotrophy.

Clumped isotope effects, a fractionation that produces $\gamma < 1$, can be thought of as double isotope effects. That is, a ^{13}C isotope effect on a D isotope effect, or a D isotope effect on a ^{13}C isotope effect. For methane molecules, the zero-point energy shift (ΔZPE) for $^{13}C/^{12}C$ substitution in non-deuterated methane (i.e., $^{13}CH_4$ vs $^{12}CH_4$) is 29.8 cm^{-1}. In comparison, ΔZPE for $^{13}C/^{12}C$ substitution in mono-deuterated methane (i.e., $^{13}CH_3D$ vs $^{12}CH_3D$) is 31.8 cm^{-1} (Fig. 4). The physical origin of preferential stability of $^{13}CH_3D$ is the difference in these two ΔZPE values (ΔΔZPE) of 2.0 cm^{-1} (Fig. 4) (Whitehill et al., 2017). In the process of C–D bond breakage (e.g., during methane oxidation), ΔΔZPE values change with the ^{13}C–D stretching vibrational mode, resulting in the reduction of ΔΔZPE at the transition state, which leads to $\gamma < 1$, and $^{13}CH_3D$ reacts slower than the rate expected from the product rule (Whitehill et al., 2017). As D leaves from CH_4 and the C–D bond is stretched, ΔΔZPE decreases due to the longer bond length and lowered interaction between ^{13}C and D at the transition state, resulting in a smaller ΔΔZPE compared to that of the reactant CH_4 (Fig. 4). Accordingly, little to negligible intrinsic clumped isotope effect is expected ($\gamma \simeq 1$) for a reactant-like early transition state, where the initial ΔΔZPE is largely retained (Fig. 4c). In contrast, a large kinetic clumped isotope effect ($\gamma < 1$) is expected for product-like late transition state (Fig. 4b). Fig. 4 compares the transition state structures of the enzymes involved in AOM and aerobic methanotrophy, methyl coenzyme M reductase (MCR) and soluble methane monooxygenase (sMMO), respectively. Notably, the transition state for MCR has a relatively long C–H bond length of 2.6 Å and planar methyl-radical-like structure (Wongnate et al., 2016), whereas sMMO has a shorter (~1.3 Å) C–H bond length (Huang et al., 2013). The bond length difference between the two transition states is consistent with the observed clumped kinetic isotope effect.

The double isotope effect has been previously studied for enzyme kinetics using *in vitro* experiments and doubly-labeled isotopologue substrates (Scharschmidt et al., 1984; Hermes et al., 1984; Rucker and Klinman, 1999). Scharschmidt et al. (1984) studied the

carbon isotope effect during the oxidation of benzyl alcohol using a doubly-deuterated substrate (benzyl alcohol-*1,1-d*$_2$). Similarly, Hermes et al. (1984) studied the double isotope effect of formate dehydrogenase using ^{13}C–D doubly-labeled formate. They compared the carbon isotope effects for deuterated and non-deuterated reactants.

Fig. 5 compares the results of the above-mentioned enzyme assay studies on double isotope effect with those of our clumped methane measurements. Here, the carbon isotope fractionation factors for non-deuterated reactants $(k_{12}/k_{13})_H$ are compared to that of the deuterated counterpart $(k_{12}/k_{13})_D$. Note that the kinetic isotope fractionation factor is defined as ^{12}C/^{13}C (not ^{13}C/^{12}C as is commonly used in the geochemical community) to follow the convention in the enzyme community. The maximum clumped isotopologue fractionation is expected when $\Delta\Delta ZPE = 0$ cm^{-1} at the transition state. Because the clumped isotope effect of ^{13}C–D bond is 4 to 6 ‰ (Fig. 6), the maximum clumped isotopologue fractionation is 4 to 6 ‰ (i.e., $(k_{12}/k_{13})_D \simeq (1.004 \text{ to } 1.006) \times (k_{12}/k_{13})_H$). This analysis does not consider tunneling effect that would potentially produce additional non-canonical effects that apparently produce further departure of γ value from unity (e.g., Young et al., 2017). It can be seen that formate dehydrogenase reactions do not produce a clumped isotopologue effect ($\gamma \simeq 1$, i.e., $(k_{12}/k_{13})_D \simeq (k_{12}/k_{13})_H$), suggesting a reactant-like transition state. In contrast, the clumped effect ($\gamma<1$) is fully expressed for alcohol dehydrogenase, suggesting a product-like transition state. As a doubly-deuterated substrate is used for experiments by Scharschmidt et al. (1984), there could also be a secondary deuterium isotope effect (when D does not participate in bond breaking) for the alcohol dehydrogenase experiments. Similarly, there is a strong clumped isotope effect for AOM but no clumped effect for aerobic methane oxidation and gas phase oxidation by OH radicals, and a relatively small clumped effect for oxidation by Cl radicals (Fig. 5).

4.3 Clumped isotopologues as tracer of methane oxidation processes

4.3.1 Methane isotopologue compositions as a result of kinetic fractionations

Major sinks of methane in the environment include atmospheric oxidation by OH and Cl radicals, and the aerobic and anaerobic microbial oxidation of methane. If these reactions impart characteristic isotope fractionation signals, the resulting methane isotope ratios can be used to partition these processes (Whitehill et al.,2017; Haghnegahdar et al.,

2017). For example, $^{2}\alpha/^{13}\alpha$ ratio for gas phase oxidation by OH radicals is ~58, which is distinctively different from the ratio for aerobic microbial oxidation of methane between 6 and 15 (e.g., Whiticar and Schaefer 2007; Wang et al., 2016). Thus, $\delta^{13}C$ and δD values of methane can be used to decouple gas phase versus microbial oxidation processes (e.g., Kai et al., 2011; Rigby et al., 2012). Experimentally measured $^{2}\alpha/^{13}\alpha$ ratios for AOM and aerobic methane oxidation, however, overlap, showing that these ratios may not be able to distinguish aerobic versus anaerobic methanotrophy (Fig. 2). Our experiments demonstrated that AOM produces distinct $\Delta^{13}CH_3D$ (and likely $\Delta^{12}CH_2D_2$) trajectories that are very different from aerobic methane oxidation and gas phase oxidation of methane (Fig. 3).

What is the range of isotopologue compositions of methane in nature when methane is produced by methanogens and consumed by AOM? Below we show that the wide range of isotopologue compositions of methane are expected from available experimental data for methanogens (Stolper et al, 2015; Gruen et al.,2018; Young et al., 2017) and AOM (this study). The relatively narrow range of observed $\delta^{13}C$, δD, and $\Delta^{13}CH_3D$ values of methane in marine environment (where AOM occurs) suggests the importance of equilibrium fractionation, as opposed to two kinetic fractionations.

In the simplest case, when the rate of methane production equals consumption by AOM (i.e., at a steady state), the isotopologue composition of methane is determined by the ratio of isotope fractionations by methanogenesis (α_{mtg}) and AOM (α_{AOM}).

$$\delta^{13}C_{CH4} = \frac{^{13}\alpha_{mtg}}{^{13}\alpha_{AOM}}(\delta^{13}C_{CO2} + 1) - 1 \quad \text{, and} \tag{9}$$

$$\delta D_{CH4} = \frac{^{2}\alpha_{mtg}}{^{2}\alpha_{AOM}}(\delta D_{H2O} + 1) - 1 \quad . \tag{10}$$

Using a typical range of $^{13}\alpha_{mtg}$ values of 0.97 to 0.92 for laboratory cultures of hydrogenotrophic methanogens (e.g., Botz et al., 1997; Okumura et al., 2016) and $^{13}\alpha_{AOM}$ of 0.97 to 0.99 (Table 2 and Holler et al., 2009), steady state $\delta^{13}C_{CH4}$ ranges from 0 to –70 ‰ relative to $\delta^{13}C_{CO2}$. The higher end is comparable to methane equilibrated at near ambient temperatures (Fig. 6). Similarly, a typical $^{2}\alpha_{mtg}$ value of 0.73 to 0.66 (low pH_2 experiments by Okumura et al., 2016), and $^{2}\alpha_{AOM}$ values from 0.76 to 0.90 (Table 2 and Holler et al., 2009) yield δD_{CH4} of –40 to –270 ‰ relative to δD_{H2O}. This range

encompasses the observed value of δD = –200 to –150 ‰ for methane in marine environment (e.g., Whiticar, 1999, Okumura et al., 2016).

The value of $\Delta^{13}CH_3D$ of methane under a steady state is simply:

$$\Delta^{13}\mathrm{CH_3D} = \ln(\gamma_{mtg}) - \ln(\gamma_{AOM}) \quad (11)$$

The $\ln(\gamma_{AOM})$ values from this study (–4.8 to –12.8 ‰, Table 2) and experimentally derived $\ln(\gamma_{mtg})$ values of –3.8 to +2.3 ‰ for hydrogenotrophic methanogenesis (Gruen et al., 2018; Douglas et al., 2020) yield the range of the $\Delta^{13}CH_3D$ value from +1.0 to +15.1 ‰. Most environmental data show $\Delta^{13}CH_3D$ values smaller than ca. 7‰, corresponding to apparent equilibrium temperatures of ca. –12 °C (e.g., Stolper et al., 2015; Wang et al., 2015; Douglas et al., 2017). The values of $\Delta^{13}CH_3D$ higher than 7‰ are uncommon but can be interpreted as a result of mixing (Douglas et al., 2017). Since mixing is non-linear for $\Delta^{13}CH_3D$, mixing of two pools of methane with different $\delta^{13}C$ and δD values can produce methane with a $\Delta^{13}CH_3D$ value that is outside of the two $\Delta^{13}CH_3D$ values of original methane. The observed relatively narrow range of $\Delta^{13}CH_3D$ values, therefore, argues for the importance of equilibrium, as opposed to kinetic fractionation for methane in marine environments.

4.3.2 Methane isotopologue compositions as a result of equilibrium fractionations

Recent studies linked near-equilibrium clumped isotopologue signals (both $\Delta^{13}CH_3D$ and $\Delta^{12}CH_2D_2$) of methane in shallow marine sediment porewater (Ash et al., 2019) and deep fracture fluids to AOM (Giunta et al., 2019). For the Baltic Sea site, Ash et al (2019) observed kinetic $\Delta^{13}CH_3D$ and ΔCH_2D_2 values (i.e., lower than expected for equilibrium) in shallow <20 m sediments. Both $\Delta^{13}CH_3D$ and ΔCH_2D_2 values increased with depth where AOM is expected. This is consistent with our results that AOM increased the $\Delta^{13}CH_3D$ value. The environmental study of Ash et al. (2019), however, is not conclusive about equilibrium vs. kinetic control for the observed isotope effects. This is because if we had stopped our experiments at f >0.5, then we would not be able to demonstrate if our data resulted from equilibrium or kinetic isotope effects. Similarly, it is uncertain whether $\Delta^{13}CH_3D$ values exceeding those of equilibration would appear deeper in the sediment studied by Ash et al. (2019). Such a signal would indicate kinetic isotopologue fractionations.

462 The estimated rate of AOM for Baltic Sea site studied by Ash et al. 2019 (0.84 pmol
463 CH_4 cm^{-3} day^{-1}, Dijkstra et al., 2018) is at the low end for marine subsurface sulfate
464 methane transition zone (Sivan et al., 2007; Knittel and Boetius, 2009) and appears under
465 low sulfate concentrations (<1 mM), which strongly influence the isotope effects of AOM
466 (Yoshinaga et al., 2014). In comparison, the rate for our AOM culture is much faster (about
467 150 nmol cm^{-3} medium day^{-1}). A faster rate of AOM at high sulfate concentrations and
468 therefore higher thermodynamic drive likely contributed kinetic signals observed in this
469 study. While the results of this study demonstrate that AOM does not always produce near-
470 equilibrium signals, it remains to be tested if and under what conditions AOM (and
471 methanogenesis) produces equilibrium signals.
472 Here, we consider methane isotopologue fractionation in nature, in particular that
473 found in marine environment, as a result of equilibrium fractionation by reversible
474 enzymatic processes. Hydrogenotrophic methanogenesis is a seven-step reaction involving
475 the transfer of eight electrons (Fig. 6). ANME carries most enzymes involved in
476 methanogenesis, and is thought to carry out the reverse reaction of methanogenesis (e.g.,
477 Hallam et al., 2004). The last step of methanogenesis, the reduction of methyl-S-CoM, is
478 catalyzed by MCR:

479 $$CH_3\text{-S-CoM} + \text{HS-CoB} \leftrightarrow CH_4 + \text{CoM-S-S-CoB} \quad (12)$$

480 where CoB and CoM-S-S-CoB are coenzyme B and heterodisulfide complex, respectively.
481 The reverse reaction is the first step for AOM. For methanogenesis, the reaction is
482 exergonic at physiological concentrations so that the reaction is favored toward the product
483 methane (e.g., Scheller et al., 2010, 2013; Thauer, 2011). The first step of methanogenesis,
484 the reduction of CO_2 to formyl-MFR, in contrast, is highly endergonic, and requires a
485 potential as low as –500 mV Eh, which is much lower than the potential set by the H_2/H^+
486 (–400 mV Eh at 1 bar pH_2 at pH=7, which is a rare condition) (Thauer et al., 2008). One
487 way of achieving this low redox potential is by coupling the highly exergonic last step of
488 methanogenesis (equation-12) to the endergonic CO_2 activation step in a so-called electron
489 bifurcation reaction (Kaster et al., 2011; Thauer et al., 2010).
490 The exergonic nature of the last step of methanogenesis can explain kinetic δD and
491 $\Delta^{13}CH_3D$ isotope fractionations observed in methanogen culture experiments, which are

often carried out at high pH_2 (>1 bar pH_2) (Gruen et al., 2018; Okumura et al., 2016; Valentine et al., 2004). Fig. 6 shows equilibrium $^{13}C/^{12}C$, D/H and ^{13}C-D isotope compositions estimated from *ab initio* calculations (for details see Appendix B). If the addition of the third-H, reduction of CH_2=H_4MPT (methylene tetrahydromethanopterin) to CH_3-H_4MPT, is reversible (as suggested by Stolper et al., 2015), methyl-H of methyl-S-CoM would be isotopically equilibrated with water and result in $\delta D = -126‰$ (when $\delta D_{H2O} = 0‰$). The fourth (i.e., the last) H addition is exergonic and produces a large kinetic isotope effect under most physiological conditions. The resulting δD value of methane can be derived as:

$$\delta D_{CH4} = ¾ \cdot {}^2\alpha_S \, (\delta D_{CH3}+1) + ¼ \cdot {}^2\alpha_p \, (\delta D_{H2O}+1) \, -1 = -374 ‰ \qquad (13)$$

where $^2\alpha_S$ and $^2\alpha_p$ are secondary and primary kinetic isotope fractionation factors, respectively (Gruen et al. 2018; Wang et al., 2015). We use $^2\alpha_p$ of 0.3 and $^2\alpha_S$ of 0.84 from Scheller et al. (2013). This simple analysis shows that kinetic δD value of –374‰ is due to three moderately D-depleted H atoms from methyl-CoM of –266‰ with one highly D-depleted (–700‰) H added during the last step of methanogenesis. The value of –374‰ is within the range (–300 to –400 ‰) commonly observed for laboratory cultures of methanogens (Okumura et al., 2016; Valentine et al., 2004). For clumped isotopologues, the last step of methanogenesis was also proposed to be responsible for low and kinetic $\Delta^{13}CH_3D$ (and δD) values (Gruen et al., 2018; Stolper et al., 2015). One study showed that kinetic $\Delta^{13}CH_3D$ values are not specific to the metabolic pathways of methanogenesis (e.g., acetoclastic vs. hydrogenotrophic), suggesting that they are produced during enzymatic reactions common in all methanogenic pathways, such as the reduction of methyl-CoM (Gruen et al., 2018). Another study, however, measured different isotopologue signals in $^{13}CH_3D$ and $^{12}CH_2D_2$ for different pathways of methanogenesis (Young et al., 2017). The different observations could be related to the source of methyl group substrates. Thus, the question remains open regarding the significance of pathways in determining the methane isotopologue compositions.

The reverse of reaction (12) is the first step of AOM, and limits the rate of AOM because, under usual physiological conditions, the reaction is favored towards methane production (e.g., Thauer, 2011). It has been shown that ANME contains high

concentrations of MCR to increase the rate of reaction (Heller et al., 2008; Shima and Thauer, 2005). When the reaction (12) in AOM is rate limiting and reversible, it would lead to D/H isotope as well as $^{13}CH_3D$ isotopologue equilibria. Here, the last H in methane is derived from HS-coenzyme B, whose H isotope ratio is likely to be equilibrated with water because of a generally weak S-H bonds. Therefore, there is a good reason to suspect that AOM will drive the isotopologue signals of the remaining methane towards equilibrium of $\delta D \simeq -197$ ‰ and $\Delta^{13}CH_3D \simeq 5.9$‰ (at ambient temperatures) when the first step of AOM is highly reversible (Fig. 6). The kinetic D- and $^{13}CH_3D$ signals observed in this study suggest that the first step of AOM was not fully reversible under our experimental conditions. It is possible that reversibility of AOM is linked to sulfate concentrations so that experiments with low sulfate concentrations may produce equilibrium $\Delta^{13}CH_3D$ values. This, however, remains to be experimentally verified.

Using ^{14}C spiked methane, Holler et al. (2011b) measured the reversibility of AOM cultures between 5 and 13%. The reversibility measured by ^{14}C represents the reversibility of the entire reactions from CO_2 and CH_4 during AOM. In contrast, equilibrium δD and $\Delta^{13}CH_3D$ values can be achieved by the reversibility of only the first step of AOM. Although our results for D- and N-series experiments are preliminary, 60% reversibility of the first step of AOM is possible. The reversibility of this first step of AOM should be tested in future experiments.

5 Conclusions

Fractionations of methane isotopologues during the anaerobic oxidation of methane (AOM) were investigated experimentally with sediment-free cultures of ANME-1 archaea and partner bacteria. The AOM in our experiments produced kinetic isotope fractionations of 11.1 to 18.3 ‰ and 117 to 180 ‰ for ^{13}C and D, respectively, where residual methane is enriched in ^{13}C and D relative to ^{12}C and ^{1}H. The clumped isotopologue, $^{13}CH_3D$, also followed kinetic fractionation, where $\Delta^{13}CH_3D$ values increased up to 8.4‰, which is above the value expected for isotopologue equilibrium. Experiments to test the effect of δD values of medium water were inconclusive about the reversibility of AOM. Previous laboratory culture experiments of methanogenic microbes have exclusively produced

lower $\Delta^{13}CH_3D$ signals than those expected for equilibrium at their growth temperatures. Our results demonstrate that AOM increases the $\Delta^{13}CH_3D$ value and produces low apparent temperature signals for remaining methane, and can explain the range of $\Delta^{13}CH_3D$ values measured for methane in natural environments.

Acknowledgements:

We thank associate editor, Ann Pearson, and three anonymous reviewers for constructive comments that significantly improve the manuscript, and Susanne Menger and Martina Alisch for the assistance in cultivation, in experiments and geochemical measurements. This work was supported by the NASA Astrobiology Institute "Rock-Powered Life" project under cooperative agreement NNA15BB02A, NSF-Geobiology and Low Temperature Geochemistry, EAR-1852946, N. Braunsdorf and D. Smit of Shell PTI/EG, and the Deep Carbon Observatory (to S.O.). J.H.R. was also supported by the Grayce B. Kerr Fellowship, the Robert R. Shrock Fellowship and the Callahan Dee Fellowship at MIT. D.S.G. was supported by a National Science Foundation Graduate Research Fellowship, the Neil and Anna Rasmussen Foundation Fund, the Grayce B. Kerr Fellowship, and a Shell-MIT Energy Initiative Graduate Fellowship. G. W. was supported by the DFG cluster of Excellence EXC 2077 'The Ocean Floor – Earth's Uncharted Interface' at MARUM, University Bremen and the Max Planck Society.

Appendix

Appendix A: A modified Rayleigh equation that includes a reversible reaction

The potential effect of reversibility for the derived fractionation factor (α) and the δD value of medium water was evaluated by constructing a modified Rayleigh fractionation model that includes internal reversibility during the first step of AOM, as the scheme shown in Fig. A1. The model does not track the reaction beyond CH_3-S-CoM due to uncertain isotope fractionation factors for subsequent reactions. Although incomplete, this model approach enables reasonable complexity and reduces the number of unknown variables.

Continuity equations for the reaction scheme in Fig. A1 can be written as:

$$\frac{dx_1}{dt} = -k_1 x_1 + k_2 y_1 \quad \text{(A1)}$$

$$\frac{dy_1}{dt} = k_1 x_1 - (k_2 + k_3) y_1 \quad \text{(A2)}$$

$$\frac{dx_2}{dt} = -\left(\frac{1}{4}\alpha_{1p} + \frac{3}{4}\alpha_{1s}\right) k_1 x_2 + \alpha_{2p} k_2 d_H y_1 + \alpha_{2s} k_2 y_2 \quad \text{(A3)}$$

$$\frac{dy_2}{dt} = -\frac{3}{4}\alpha_{1s} k_1 x_2 + \left[\alpha_{2s} k_2 + \left(\frac{1}{3}\alpha_{3p} + \frac{2}{3}\alpha_{3s}\right) k_3\right] y_2 \quad \text{(A4)}$$

where, x_1, x_2, y_1, and y_2 are concentrations for CH_4, CH_3D, CH_3-S-CoM and CH_2D-S-CoM, respectively, and k_n (n=1, 2, or 3) are the first order rate constants for non-deuterated isotopologues, and α_{np} and α_{ns} are the primary and secondary isotope fractionation factors, corresponding to the rate constant, k_n. For natural D abundance, the flux from CH_3D to CH_4 is ignored for the mass-balance of CH_3-S-CoM. This simplifies the equation A2 and subsequent solutions without affecting the results.

Assuming steady states for intermediate species (i.e., $dy_1/dt = dy_2/dt = 0$), differential equations (A1) to (A4) can be reduced to:

$$\frac{dx_1}{dt} = a x_1 \quad \text{(A5)}$$

$$\frac{dx_2}{dt} = b x_1 + c x_2 \quad \text{(A6)}$$

Where,

$$a = -k_1 \phi \quad \text{(A7)}$$

$$b = \alpha_{2p} d_H k_1 (1 - \phi) \quad \text{(A8)}$$

$$c = -k_1 \left[\left(\frac{1}{4}\alpha_{1p} + \frac{3}{4}\alpha_{1s}\right) + \frac{3}{4}\frac{\alpha_{1s}\alpha_{2s}(1-\phi)}{\alpha_{2s}(1-\phi) + \left(\frac{1}{3}\alpha_{3p} + \frac{2}{3}\alpha_{3s}\right)\phi}\right] x_2 \quad \text{(A9)}$$

and ϕ is the forward commitment defined as (e.g. Singh et al., 2016):

$$\phi = \frac{k_3}{k_2 + k_3} \quad \text{(A10)}$$

598 The value of ϕ varies from 1 to 0 for unidirectional to fully reversible reactions,
599 respectively. This parameterization avoids the value of ϕ becoming infinity (as opposed to
600 defining $\phi=k_2/k_3$). The analytical solutions for the differential equations (A5) and (A6) are:
601

$$x_1(t) = x_1^i e^{at} \tag{A11}$$

$$x_2(t) = x_1^i \frac{b}{a-c}\, e^{at} + \left(x_2^i - x_1^i \frac{b}{a-c}\right) e^{ct} \tag{A12}$$

602 where, x_1^i and x_2^i are initial concentrations. Equations A11 and A12 are used to derive an
603 analytical solution for the δD value of methane as a function of fraction remaining, f (=
604 exp(at)):
605

$$\delta D + 1 = \frac{\omega}{R_i} + \left(1 - \frac{\omega}{R_i}\right) f^{\theta-1} \tag{A13}$$

606 where $\omega = b/(a\text{-}c)$ and $\theta = c/a$ (in equations A7, A8 and A9), and R_i is the isotopologue ratio
607 (CH_3D/CH_4) at t=0. Note that the ratio is four times that of bulk D/H ratio of methane
608 because of the symmetric factors. Equation (A13) compares the analytical solution for the
609 reaction scheme in Fig. A1 with that of the conventional Rayleigh equation.
610 We applied the equation (A13) to fit δD data for D- and N-series experiments to
611 examine the potential impact of δD values of medium water. We assumed the secondary
612 isotope effects (α_{1s}, α_{2s}, and α_{3s}) of 0.85 (following Scheller et al., 2013), and fit the data
613 with two fitting parameters, α_{1p} (assumed equal to α_{3p}), and ϕ. The value of α_{2p} was
614 constrained by α_{1p} and the equilibrium fractionation between CH_4 and CH_3-S-CoM in Fig.
615 6. The MATLAB script of the model is available in Electronic Annex. The best fit to the
616 data was obtained for $\alpha_{1p} = \alpha_{3p} = 0.823$ and $\phi = 0.40$ (Figure A1), suggesting a potentially
617 substantial reversibility for the reaction (i.e., back flux is 60% of the forward flux). This
618 model, however, is highly preliminary because of the lack of data for control experiments
619 (N-series) at later time points of the experiments (f <0.5, Fig. 1e). We recognize that this
620 is important area of future research, and we present this model in order to aid the design of
621 future experiments. We suggest that the best approach would use water with more distinct
622 δD values by spiking with D_2O and taking data for later time steps, where the effect of
623 reversibility is better expressed than in earlier time steps.

Appendix B: Estimation of equilibrium fractionations

Equilibrium fractionations shown in Fig. 6 were estimated by calculating reduced partition function ratios following the conventional formula (e.g., Bigeleisen and Mayer, 1947; Urey, 1947). Normal mode frequencies were estimated by molecular simulation by B3LYP with the 6-311+G** basis set using GAMESS software (Gordon and Schmidt, 2005). Reduced partition function ratios for intermediate compounds were approximated by simple molecules, in which the same number of H, N, O, and S-atoms are bound to the C atom that contains the C-H bonds in question. We used following compounds as analogues: formamide (for CHO-MFR in Fig. 6), pyrimidine (for CH=H_4MPT), methylenediamine (for CH_2=H_4MPT), methylamine (for CH_3-H_4MPT), and methanethiol (for CH_3-S-CoM). Discussion for the accuracy for using these "cutoff" model can be found in Heskey and Schowen (1983) and Rucker and Klinman (1999). The results of the calculation should be taken as a first order approximation because of a number of assumptions made. In addition to the use of cutoff molecules, our calculation assumed gas phase molecules and harmonic oscillators. For D/H isotope fractionation, in particular, anharmonic effect and solvation are expected to be important (Richet et al., 1977; Wang et al., 2009). These effects, however, tend to cancel out when comparing fractionation factors estimated by the same computational method such that relative fractionation factors among modeled compounds can be accurate (Wang et al., 2009). We used the experimental fractionation factor for H_2O(gas)/H_2O(liquid) of Horita and Wesolowski (1994) and calculated the fractionation factor for C-H compounds against H_2O(gas) to derive the equilibrium fractionation factor against liquid H_2O. For clumped isotope effect, anharmonic effects can produce about 0.3‰ bias for $\Delta^{13}CH_3D$ at a temperature below ca. 100 °C but estimates form different levels of theory agree well (Liu and Liu, 2016; Webb and Miller, 2014).

652
653 **References**

654 Ash J. L., Egger M., Treude T., Kohl I., Cragg B., Parkes R. J., Slomp C. P., Lollar B. S.
655 and Young E. D. (2019) Exchange catalysis during anaerobic methanotrophy revealed
656 by $^{12}CH_2D_2$ and $^{13}CH_3D$ in methane. *Geochemical Perspect. Lett.* **10**, 26–30.

657 Bigeleisen J. (1955) Statistical mechanics of isotopic systems with small quantum
658 corrections. I. General considerations and the rule of the geometric mean. *J. Chem.*
659 *Phys.* **23**, 2264–2267.

660 Bigeleisen J. and Mayer M. G. (1947) Calculation of equilibrium constants for isotopic
661 exchange reactions. *J. Chem. Phys.* **15**, 261–267.

662 Botz R., Pokojski H. D., Schmitt M. and Thomm M. (1997) Carbon isotope fractionation
663 during bacterial methanogenesis by CO_2 reduction. *Org. Geochem.* **25**, 255–262.

664 Borowski W. S., Paull C. K. and Ussier W. (1997) Carbon cycling within the upper
665 methanogenic zone of continental rise sediments: An example from the methane-rich
666 sediments overlying the blake ridge gas hydrate deposits. *Mar. Chem.* **57**, 299–311.

667 Buffett B. and Archer D. (2004) Global inventory of methane clathrate: Sensitivity to
668 changes in the deep ocean. *Earth Planet. Sci. Lett.* **227**, 185–199.

669 Canfield D. E. and Thamdrup B. (1994) The production of 34S-depleted sulfide during
670 bacterial disproportionation of elemental sulfur. *Science* **266**, 1973–1975.

671 Coleman D. D., Risatti J. B. and Schoell M. (1981) Fractionation of carbon and hydrogen
672 isotopes by methane-oxidizing bacteria. *Geochim. Cosmochim. Acta* **45**, 1033–1037.

673 Coplen T. B. (2011) Guidelines and recommended terms for expression of stable-isotope-
674 ratio and gas-ratio measurement results. *Rapid Commun. Mass Spectrom.* **25**, 2538–
675 2560.

676 Cord-Ruwisch R. (1985) A quick method for the determination of dissolved and
677 precipitated sulfides in cultures of sulfate-reducing bacteria. *J. Microbiol. Methods* **4**,
678 33–36.

679 Dijkstra N., Hagens M., Egger M. and Slomp C. P. (2018) Post-depositional formation of
680 vivianite-type minerals alters sediment phosphorus records. *Biogeosciences* **15**, 861–
681 883.

682 Douglas P. M. J., Stolper D. A., Eiler J. M., Sessions A. L., Lawson M., Shuai Y., Bishop
683 A., Podlaha O. G., Ferreira A. A., Santos Neto E. V., Niemann M., Steen A. S., Huang
684 L., Chimiak L., Valentine D. L., Fiebig J., Luhmann A. J., Seyfried W. E., Etiope G.,
685 Schoell M., Inskeep W. P., Moran J. J. and Kitchen N. (2017) Methane clumped
686 isotopes: Progress and potential for a new isotopic tracer. *Org. Geochem.* **113**, 262–
687 282.
688 Douglas P. M. J., Gonzalez Moguel R., Walter Anthony K. M., Wik M., Crill P. M.,
689 Dawson K. S., Smith D. A., Yanay E., Lloyd M. K., Stolper D. A., Eiler J. M. and
690 Sessions A. L. (2020) Clumped isotopes link older carbon substrates with slower
691 rates of methanogenesis in northern lakes. *Geophys. Res. Lett.* **47**, 1–10.
692 Eldridge D. L., Korol R., Lloyd M. K., Turner A. C., Webb M. A., Miller T. F. and
693 Stolper D. A. (2019) Comparison of experimental vs theoretical abundances of
694 $^{13}CH_3D$ and $^{12}CH_2D_2$ for isotopically equilibrated systems from 1 to 500 °C. *ACS*
695 *Earth Sp. Chem.* **3**, 2747–2764.
696 Giunta T., Young E. D., Warr O., Kohl I., Ash J. L., Martini A., Mundle S. O. C., Rumble
697 D., Pérez-Rodríguez I., Wasley M., LaRowe D. E., Gilbert A. and Sherwood Lollar B.
698 (2019) Methane sources and sinks in continental sedimentary systems: New insights
699 from paired clumped isotopologues $^{13}CH_3D$ and $^{12}CH_2D_2$. *Geochim. Cosmochim. Acta*
700 **245**, 327–351.
701 Gordon M. S. and Schmidt M. W. (2005) Advances in electronic structure theory:
702 GAMESS a decade later. *Theory Appl. Comput. Chem.*, 1167–1189
703 Gruen D. S., Wang D. T., Könneke M., Topçuoğlu B. D., Stewart L. C., Goldhammer T.,
704 Holden J. F., Hinrichs K.-U. and Ono S. (2018) Experimental investigation on the
705 controls of clumped isotopologue and hydrogen isotope ratios in microbial methane.
706 *Geochim. Cosmochim. Acta* **237**, 339–356.
707 Haghnegahdar M. A., Schauble E. A. and Young E. D. (2017) A model for $^{12}CH_2D_2$ and
708 $^{13}CH_3D$ as complementary tracers for the budget of atmospheric CH_4. *Global*
709 *Biogeochem. Cycles* **31**, 1387–1407.
710 Hallam S. J., Putnam N., Preston C. M., Detter J. C., Rokhsar D., Richardson P. H. and
711 DeLong E. F. (2004) Reverse methanogenesis: Testing the hypothesis with
712 environmental genomics. *Science* **305**, 1457–1462.

713 Heller C., Hoppert M. and Reitner J. (2008) Immunological localization of coenzyme M
714 reductase in anaerobic methane-oxidizing archaea of ANME 1 and ANME 2 type.
715 *Geomicrobiol. J.* **25**, 149–156.
716 Hermes J. D., Morrical S. W., O'Leary M. H. and Cleland W. W. (1984) Variation of
717 transition-state structure as a function of the nucleotide in reactions catalyzed by
718 dehydrogenases. 2. Formate dehydrogenase. *Biochemistry* **23**, 5479–5488.
719 Heskey P. W. and Schowen R. L. (1983) Reaction-coordinate tunneling in hydrite-transfer
720 reactions. *J. Am. Chem. Soc.* **105**, 5704–5706.
721 Holler T., Wegener G., Knittel K., Boetius A., Brunner B., Kuypers M. M. M. and Widdel
722 F. (2009) Substantial $^{13}C/^{12}C$ and D/H fractionation during anaerobic oxidation of
723 methane by marine consortia enriched in vitro. *Environ. Microbiol. Rep.* **1**, 370–376.
724 Holler T., Widdel F., Knittel K., Amann R., Kellermann M.Y., Hinrichs K.U., Teske A.,
725 Boetius A. and Wegener G. (2011a) Thermophilic anaerobic oxidation of methane by
726 marine microbial consortia. *ISME J.* **5**(12), 1946-56.
727 Holler T., Wegener G., Niemann H., Deusner C., Ferdelman T. G., Boetius A., Brunner B.
728 and Widdel F. (2011b) Carbon and sulfur back flux during anaerobic microbial
729 oxidation of methane and coupled sulfate reduction. *Proc. Natl. Acad. Sci. U. S. A.*
730 **108**, 1484-1490.
731 Horita J. and Wesolowski D. J. (1994) Liquid-vapor fractionation of oxygen and hydrogen
732 isotopes of water from the freezing to the critical temperature. *Geochim. Cosmochim.*
733 *Acta* **58**, 3425–3437.
734 Huang S. P., Shiota Y. and Yoshizawa K. (2013) DFT study of the mechanism for methane
735 hydroxylation by soluble methane monooxygenase (sMMO): Effects of oxidation
736 state, spin state, and coordination number. *Dalt. Trans.* **42**, 1011–1023.
737 Inagaki F., Hinrichs K. U., Kubo Y., Bowles M. W., Heuer V. B., Hong W. L., Hoshino
738 T., Ijiri A., Imachi H., Ito M., Kaneko M., Lever M. A., Lin Y. S., Methé B. A., Morita
739 S., Morono Y., Tanikawa W., Bihan M., Bowden S. A., Elvert M., Glombitza C.,
740 Gross D., Harrington G. J., Hori T., Li K., Limmer D., Liu C. H., Murayama M.,
741 Ohkouchi N., Ono S., Park Y. S., Phillips S. C., Prieto-Mollar X., Purkey M.,
742 Riedinger N., Sanada Y., Sauvage J., Snyder G., Susilawati R., Takano Y., Tasumi E.,
743 Terada T., Tomaru H., Trembath-Reichert E., Wang D. T. and Yamada Y. (2015)

744 Exploring deep microbial life in coal-bearing sediment down to ~2.5 km below the
745 ocean floor. *Science* **349**, 420–424.
746 Joelsson L. M. T., Forecast R., Schmidt J. A., Meusinger C., Nilsson E. J. K., Ono S. and
747 Johnson M. S. (2014) Relative rate study of the kinetic isotope effect in the $^{13}CH_3D$ +
748 Cl reaction. *Chem. Phys. Lett.* **605–606**, 152–157.
749 Joelsson L. M. T., Schmidt J. A., Nilsson E. J. K., Blunier T., Griffith D. W. T., Ono S.
750 and Johnson M. S. (2016) Kinetic isotope effects of $^{12}CH_3D$+OH and $^{13}CH_3D$+OH
751 from 278 to 313K. *Atmos. Chem. Phys.* **16**, 4439–4449.
752 Kai F. M., Tyler S. C., Randerson J. T. and Blake D. R. (2011) Reduced methane growth
753 rate explained by decreased Northern Hemisphere microbial sources. *Nature* **476**, 194.
754 Kaster A. K., Moll J., Parey K. and Thauer R. K. (2011) Coupling of ferredoxin and
755 heterodisulfide reduction via electron bifurcation in hydrogenotrophic methanogenic
756 archaea. *Proc. Natl. Acad. Sci. U. S. A.* **108**, 2981–2986.
757 Kinnaman F. S., Valentine D. L. and Tyler S. C. (2007) Carbon and hydrogen isotope
758 fractionation associated with the aerobic microbial oxidation of methane, ethane,
759 propane and butane. *Geochim. Cosmochim. Acta* **71**, 271–283.
760 Klein F., Grozeva N. G. and Seewald J. S. (2019) Abiotic methane synthesis and
761 serpentinization in olivine-hosted fluid inclusions. *Proc. Natl. Acad. Sci.* **116**, 17666–
762 17672.
763 Knittel K. and Boetius A. (2009) Anaerobic oxidation of methane: Progress with an
764 unknown process. *Annu. Rev. Microbiol.* **63**, 311-34.
765 Knittel K., Wegener G. and Boetius A. (2019) Anaerobic methane oxidizers. in: Microbial
766 communities utilizing hydrocarbons and lipids: Members, metagenomics and
767 ecophysiology, (Ed.) T.J. McGenity, Springer International Publishing. Cham, pp.
768 113-132.
769 Krukenberg V., Riedel D., Gruber-Vodicka H. R., Buttigieg P. L., Tegetmeyer H. E.,
770 Boetius A. and Wegener G. (2018) Gene expression and ultrastructure of meso- and
771 thermophilic methanotrophic consortia. *Environ. Microbiol.* **20**, 1651–1666.
772 Laso-Pérez R., Krukenberg V., Musat F. and Wegener G. (2018) Establishing anaerobic
773 hydrocarbon-degrading enrichment cultures of microorganisms under strictly anoxic
774 conditions. *Nature Protocols* **13**, 1310–1330.

775 Liu Q. and Liu Y. (2016) Clumped-isotope signatures at equilibrium of CH4, NH3, H2O,
776 H2S and SO2. *Geochim. Cosmochim. Acta* **175**, 252–270.
777 Marlow J. J., Steele J. A., Ziebis W., Scheller S., Case D., Reynard L. M. and Orphan V.
778 J. (2017) Monodeuterated methane, an isotopic tool to assess biological methane
779 metabolism rates. *mSphere* **2**, 1–19.
780 Mariotti A., Germon J. C., Hubert P., Kaiser P., Letolle R., Tardieux A. and Tardieux P.
781 (1981) Experimental determination of nitrogen kinetic isotope fractionation: Some
782 principles; illustration for the denitrification and nitrification processes. *Plant Soil* **62**,
783 413–430.
784 McDermott J. M., Seewald J. S., German C. R. and Sylva S. P. (2015) Pathways for abiotic
785 organic synthesis at submarine hydrothermal fields. *Proc. Natl. Acad. Sci. U. S. A.*
786 **112**, 7668–7672.
787 Meyerdierks A., Kube M., Kostadinov I., Teeling H., Glöckner F. O., Reinhardt R. and
788 Amann R. (2010) Metagenome and mRNA expression analyses of anaerobic
789 methanotrophic archaea of the ANME-1 group. *Environ. Microbiol.* **12**, 422–439.
790 Milkov A. V. (2004) Global estimates of hydrate-bound gas in marine sediments: How
791 much is really out there? *Earth-Science Rev.* **66**, 183–197.
792 Okumura T., Kawagucci S., Saito Y., Matsui Y., Takai K. and Imachi H. (2016) Hydrogen
793 and carbon isotope systematics in hydrogenotrophic methanogenesis under H_2-limited
794 and H_2-enriched conditions: Implications for the origin of methane and its isotopic
795 diagnosis. *Prog. Earth Planet. Sci.* **3**, 2–15.
796 Ono S., Wang D. T., Gruen D. S., Sherwood Lollar B., Zahniser M. S., McManus B. J. and
797 Nelson D. D. (2014) Measurement of a doubly substituted methane isotopologue,
798 $^{13}CH_3D$, by tunable infrared laser direct absorption spectroscopy. *Anal. Chem.* **86**,
799 6487–6494.
800 Pohlman J. W., Ruppel C., Hutchinson D. R., Downer R. and Coffin R. B. (2008) Assessing
801 sulfate reduction and methane cycling in a high salinity pore water system in the
802 northern Gulf of Mexico. *Mar. Pet. Geol.* **25**, 942–951.
803 Powelson D. K., Chanton J. P. and Abichou T. (2007) Methane oxidation in biofilters
804 measured by mass-balance and stable isotope methods. *Environ. Sci. Technol.* **41**,
805 620–625.

806 Reeburgh W. S. (2007) Oceanic methane biogeochemistry. *Chem. Rev.* **107**, 486–513.
807 Richet P., Bottinga Y. and Javoy M. (1977) A Review of Hydrogen, Carbon, Nitrogen,
808 Oxygen, Sulphur, and Chlorine Stable Isotope Fractionation Among Gaseous
809 Molecules. *Annu. Rev. Earth Planet. Sci.* **5**, 65–110.
810 Rigby M., Manning A. J. and Prinn R. G. (2012) The value of high-frequency, high-
811 precision methane isotopologue measurements for source and sink estimation. *J.*
812 *Geophys. Res. Atmos.* **117**, D12312.
813 Rucker J. and Klinman J. P. (1999) Computational study of tunneling and coupled motion
814 in alcohol dehydrogenase-catalyzed reactions: Implication for measured hydrogen and
815 carbon isotope effects. *J. Am. Chem. Soc.* **121**, 1997–2006.
816 Scharschmidt M., Fisher M. A. and Cleland W. W. (1984) Variation of transition-state
817 structure as a function of the nucleotide in reactions catalyzed by dehydrogenases. 1.
818 Liver alcohol dehydrogenase with benzyl alcohol and yeast aldehyde dehydrogenase
819 with benzaldehyde. *Biochemistry* **23**, 5471–5478.
820 Scheller S., Goenrich M., Boecher R., Thauer R. K. and Jaun B. (2010) The key nickel
821 enzyme of methanogenesis catalyses the anaerobic oxidation of methane. *Nature* **465**,
822 606–608.
823 Scheller S., Goenrich M., Thauer R. K. and Jaun B. (2013) Methyl-coenzyme M reductase
824 from methanogenic archaea: Isotope effects on the formation and anaerobic oxidation
825 of methane. *J. Am. Chem. Soc.* **135**, 14975–14984.
826 Schoell M. (1980) The hydrogen and carbon isotopic composition of methane from natural
827 gases of various origins. *Geochim. Cosmochim. Acta* **44**, 649–661.
828 Shima S. and Thauer R. K. (2005) Methyl-coenzyme M reductase and the anaerobic
829 oxidation of methane in methanotrophic Archaea. *Curr. Opin. Microbiol.* **8**, 643–648.
830 Sim M. S., Bosak T. and Ono S. (2011) Large sulfur isotope fractionation does not require
831 disproportionation. *Science.* **333**, 74–77.
832 Singh P., Islam Z. and Kohen A. (2016) Examinations of the Chemical Step in Enzyme
833 Catalysis. In *Computational Approaches for Studying Enzyme Mechanism Part A*.
834 Academic Press. pp. 287–318.
835 Sivan O., Schrag D.P. and Murray R.W. (2007) Rates of methanogenesis and
836 methanotrophy in deep-sea sediments. *Geobiology* **5**, 141-151.

837 Stolper D. A., Lawson M., Davis C. L., Ferreira A. A., Santos Neto E. V., Ellis G. S.,
838 Lewan M. D., Martini A. M., Tang Y., Schoell M., Sessions A. L. and Eiler J. M.
839 (2014a) Formation temperatures of thermogenic and biogenic methane. *Science* **344**,
840 1500–1503.
841 Stolper D. A., Sessions A. L., Ferreira A. A., Santos Neto E. V., Schimmelmann A., Shusta
842 S. S., Valentine D. L. and Eiler J. M. (2014b) Combined 13C-D and D-D clumping in
843 methane: Methods and preliminary results. *Geochim. Cosmochim. Acta* **126**, 169–191.
844 Stolper D. A., Martini A. M., Clog M., Douglas P. M., Shusta S. S., Valentine D. L.,
845 Sessions A. L. and Eiler J. M. (2015) Distinguishing and understanding thermogenic
846 and biogenic sources of methane using multiply substituted isotopologues. *Geochim.*
847 *Cosmochim. Acta* **161**, 219–247.
848 Thauer R. K. (2011) Anaerobic oxidation of methane with sulfate: On the reversibility of
849 the reactions that are catalyzed by enzymes also involved in methanogenesis from
850 CO_2. *Curr. Opin. Microbiol.* **14**, 292–299.
851 Thauer R. K., Kaster A. K., Seedorf H., Buckel W. and Hedderich R. (2008) Methanogenic
852 archaea: Ecologically relevant differences in energy conservation. *Nat. Rev.*
853 *Microbiol.* **6**, 579–591.
854 Thauer R. K., Kaster A.-K., Goenrich M., Schick M., Hiromoto T. and Shima S. (2010)
855 Hydrogenases from methanogenic archaea, nickel, a novel cofactor, and H_2 storage.
856 *Annu. Rev. Biochem.* **79**, 507–536.
857 Tissot B., Durand B., Espitalie J. and Combaz A. (1974) Influence of nature and diagenesis
858 of organic matter in formation of petroleum. *Am. Assoc. Pet. Geol. Bull.* **58**, 499–506.
859 Urey H. C. (1947) The thermodynamic properties of isotopic substances. *J. Chem. Soc.*,
860 562-581.
861 Valentine D. L., Chidthaisong A., Rice A., Reeburgh W. S. and Tyler S. C. (2004) Carbon
862 and hydrogen isotope fractionation by moderately thermophilic methanogens.
863 *Geochim. Cosmochim. Acta* **68**, 1571–1590.
864 Wang D. T., Gruen D. S., Sherwood Lollar B., Hinrichs K.-U., Stewart L. C., Holden J. F.,
865 Hristov A. N., Pohlman J. W., Morrill P. L., Könneke M., Delwiche K. B., Reeves E.
866 P., Sutcliffe C. N., Ritter D. J., Seewald J. S., McIntosh J. C., Hemond H. F., Kubo M.

867 D., Cardace D., Hoehler T. M. and Ono S. (2015) Nonequilibrium clumped isotope
868 signals in microbial methane. *Science* **348**, 428-431
869 Wang D. T., Welander P. V. and Ono S. (2016) Fractionation of the methane isotopologues
870 $^{13}CH_4$, $^{12}CH_3D$, and $^{13}CH_3D$ during aerobic oxidation of methane by Methylococcus
871 capsulatus (Bath). *Geochim. Cosmochim. Acta* **192**, 186–202.
872 Wang D. T., Reeves E. P., McDermott J. M., Seewald J. S. and Ono S. (2018) Clumped
873 isotopologue constraints on the origin of methane at seafloor hot springs. *Geochim.*
874 *Cosmochim. Acta* **223**, 141–158.
875 Wang Y., Sessions A. L., Nielsen R. J. and Goddard W. A. (2009) Equilibrium $^{2}H/^{1}H$
876 fractionations in organic molecules: I. Experimental calibration of ab initio
877 calculations. *Geochim. Cosmochim. Acta* **73**, 7060–7075.
878 Webb M. A. and Miller T. F. (2014) Position-specific and clumped stable isotope studies:
879 Comparison of the urey and path-integral approaches for carbon dioxide, nitrous
880 oxide, methane, and propane. *J. Phys. Chem. A* **118**, 467–474.
881 Wegener G., Krukenberg V., Ruff S. E., Kellermann M. Y. and Knittel K. (2016) Metabolic
882 capabilities of microorganisms involved in and associated with the anaerobic oxidation
883 of methane. *Front. Microbiol.* **7**, 1–16.
884 Whitehill A. R., Joelsson L. M. T., Schmidt J. A., Wang D. T., Johnson M. S. and Ono S.
885 (2017) Clumped isotope effects during OH and Cl oxidation of methane. *Geochim.*
886 *Cosmochim. Acta* **196**, 307–325.
887 Whiticar M. J. (1999) Carbon and hydrogen isotope systematics of bacterial formation and
888 oxidation of methane. *Chem. Geol.* **161**, 291–314.
889 Whiticar M. and Schaefer H. (2007) Constraining past global tropospheric methane
890 budgets with carbon and hydrogen isotope ratios in ice. *Philos. Trans. R. Soc. A Math.*
891 *Phys. Eng. Sci.* **365**, 1793–1828.
892 Wilhelms A., Larter S. R., Head I., Farrimond P., Di-Primio R. and Zwach C. (2001)
893 Biodegradation of oil in up lifted basins prevented by deep-burial sterilization. *Nature*
894 **411**, 1034–1037.
895 Wongnate T., Sliwa D., Ginovska B., Smith D., Wolf M. W., Lehnert N., Raugei S. and
896 Ragsdale S. W. (2016) The radical mechanism of biological methane synthesis by
897 methylcoenzyme M reductase. *Science* **352**, 953–958.

York D., Evensen N. M., Martínez M. L. and De Basabe Delgado J. (2004) Unified equations for the slope, intercept, and standard errors of the best straight line. *Am. J. Phys.* **72**, 367–375.

Yoshinaga M. Y., Holler T., Goldhammer T., Wegener G., Pohlman J. W., Brunner B., Kuypers M. M. M., Hinrichs K. U. and Elvert M. (2014) Carbon isotope equilibration during sulphate-limited anaerobic oxidation of methane. *Nat. Geosci.* **7**, 190–194.

Young E. D., Kohl I. E., Lollar B. S., Etiope G., Rumble D., Li (李姝宁) S., Haghnegahdar M. A., Schauble E. A., McCain K. A., Foustoukos D. I., Sutclife C., Warr O., Ballentine C. J., Onstott T. C., Hosgormez H., Neubeck A., Marques J. M., Pérez-Rodríguez I., Rowe A. R., LaRowe D. E., Magnabosco C., Yeung L. Y., Ash J. L. and Bryndzia L. T. (2017) The relative abundances of resolved $^{12}CH_2D_2$ and $^{13}CH_3D$ and mechanisms controlling isotopic bond ordering in abiotic and biotic methane gases. *Geochim. Cosmochim. Acta* **203**, 235–264.

Table 1: Results from incubation experiments with the AOM cultures. Errors for $\Delta^{13}CH_3D$ values are 95% confidence intervals for TILDAS measurements (N = 4 to 8).

Sample ID	time (days)	CH_4 oxidized (%)	sulfide (mM)	δD_{H2O} (‰)	$\delta^{13}C_{DIC}$ (‰)	$\delta^{13}C_{CH4}$ (‰)	δD_{CH4} (‰)	$\Delta^{13}CH_3D$ (‰)
Initial CH_4 from cylinder for C and B series						-36.74	-166.02	1.63±0.64
C series								
C0	0	0.0	0.39	*n.m.*	*n.m.*	*n.m.*	*n.m.*	*n.m.*
C1	1	0.5	0.46	-48.2	-9.2	-37.12	-165.14	1.79±0.32
C2	8	8.1	1.50	-48.8	-10.3	-35.44	-153.75	2.13±0.28
C3	14	12.6	2.14	-48.7	-11.2	-34.23	-142.09	2.35±0.43
C4	21	21.5	3.36	-48.6	-12.1	-33.05	-130.19	3.05±0.46
C5	28	31.2	4.68	-48.6	-13.0	-31.16	-111.49	3.86±0.33
C6	35	34.3	5.11	-48.6	-13.4	-30.68	-108.10	4.37±0.23
C7	42	35.6	5.29	-48.6	-13.7	-29.05	-92.67	5.06±0.25
B-series								
B0	0	0.0	0.32	*n.m.*	*n.m.*	-36.90	-166.02	1.74±0.22
B1	4	5.2	1.04	-53.6	-13.3	-36.07	-158.89	2.07±0.42
B2	11	13.4	2.18	-53.5	-14.1	-34.01	-141.00	2.65±0.28
B3	18	24.1	3.64	-53.6	-16.4	-32.33	-126.44	2.98±0.18
B4	25	35.1	5.14	-53.7	-16.7	-31.19	-117.09	3.34±0.18
B5	32	43.0	6.18	-53.7	-18.0	*n.m.*	*n.m.*	*n.m.*
B6	39	46.6	6.71	-53.5	-18.6	-26.71	-80.47	4.47±0.10
B7	46	61.0	8.68	-53.5	-20.2	-21.81	-37.72	5.47±0.20
B8	54	55.0	7.86	-53.6	-19.5	*n.m.*	*n.m.*	*n.m.*
B9	60	69.9	9.86	-53.7	-20.7	-18.90	-6.39	7.07±0.22
B10	67	75.2	10.64	-53.8	-20.6	*n.m.*	*n.m.*	*n.m.*
Abiotic controls								
X1	1	n.m.	0	-48.6	-7.2	-36.82	-165.95	1.87±0.49
X2	14	n.m.	0	-48.5	-8.4	-36.68	-165.78	1.41±0.38
X3	41	n.m.	0	-48.5	-8.7	-36.31	-164.93	1.45±0.25
Initial CH_4 from cylinder for D and N series						-42.00	-189.56	2.5±0.93
D-series								
D1	0	0.0	0.44	-202.2	-17.9	-42.12	-189.82	2.67±0.29
D2	3	1.7	0.69	-199.6	-18.6	-42.00	-187.68	2.95±0.30
D3	7	7.1	1.49	-199.8	-20.1	-41.42	-182.54	3.5±0.23
D4	11	12.9	2.36	-199.9	-22.3	-40.51	-174.37	3.7±0.18
D5	15	20.9	3.56	-200.3	-24.0	-39.61	-166.58	4.1±0.32
D6	19	26.5	4.40	-200.2	-25.2	*n.m.*	*n.m.*	*n.m.*
D7	24	35.3	5.71	-199.3	-26.5	-36.89	-146.01	4.68±0.36
D8	28	49.7	7.85	-199.7	-28.3	-36.04	-138.37	5.19±0.22
D9	31	50.1	7.93	-200.6	-28.6	*n.m.*	*n.m.*	*n.m.*
D10	35	61.6	9.64	-199.4	-30.1	-32.45	-107.65	6.36±0.18
D11	49	81.8	12.65	-201.0	-31.1	-30.34	-79.77	8.46±0.21
N-series								
N1	0	0.0	0.36	-55.5	-17.8	-42.09	-189.82	2.54±0.46
N2	*n.m.*	*n.m.*	0.65	-55.0	-18.5	*n.m.*	*n.m.*	*n.m.*
N3	*7*	*7.1*	1.42	-55.0	-19.7	-41.57	-180.64	3.17±0.28
N4	*n.m.*	*n.m.*	3.20	n.m.	-23.4	*n.m.*	*n.m.*	*n.m.*
N5	24	23.6	3.89	-54.8	-24.3	-38.82	-156.82	3.35±0.33
N6	31	47.5	7.45	-55.0	-28.2	-35.28	-126.22	4.43±0.34

n.m.: not measured

Table 2: Kinetic fractionation factors calculated from experimental results.

Series	$^{13}\varepsilon$ (‰)	$^{2}\varepsilon$ (‰)	γ	1-γ (‰)
C	18.3±0.7	180.0±5.4	0.9872±0.0010	12.8±1.0
B	17.0±0.5	164.9±4.9	0.9916±0.0004	8.4±0.4
D	11.1±0.4	116.5±3.5	0.9947±0.0003	5.3±0.3
N	11.3±0.5	141.1±6.0	0.9952±0.0009	4.8±0.9

Errors are estimated for uncertainty of H_2S measurements of 5% and 95% confidence interval for isotopologue measurements. Errors for γ values are estimated by propagating errors for $^{13}\alpha$, $^{2}\alpha$ and the linear regression slope in ln(f) versus $\Delta^{13}CH_3D$ (Fig. 1) without considering covariance.

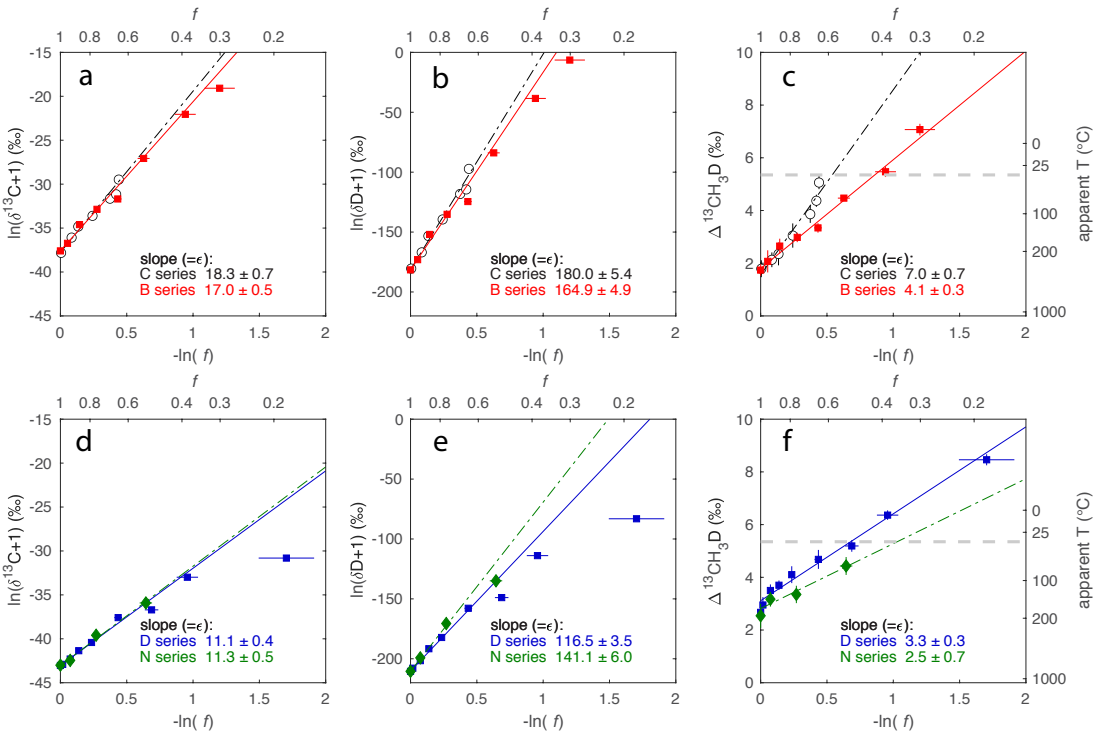

Fig. 1: Evolution of isotopologue compositions during methane consumption by AOM. Diagram (a), (b) and (c) show the results from B- and C-series (open circle and filled square, respectively), and diagrams (d), (e), and (f) show the results from D- and N-series (open square and filled diamond, respectively). The slopes for least square fits are representing ε values and shown in the diagram.

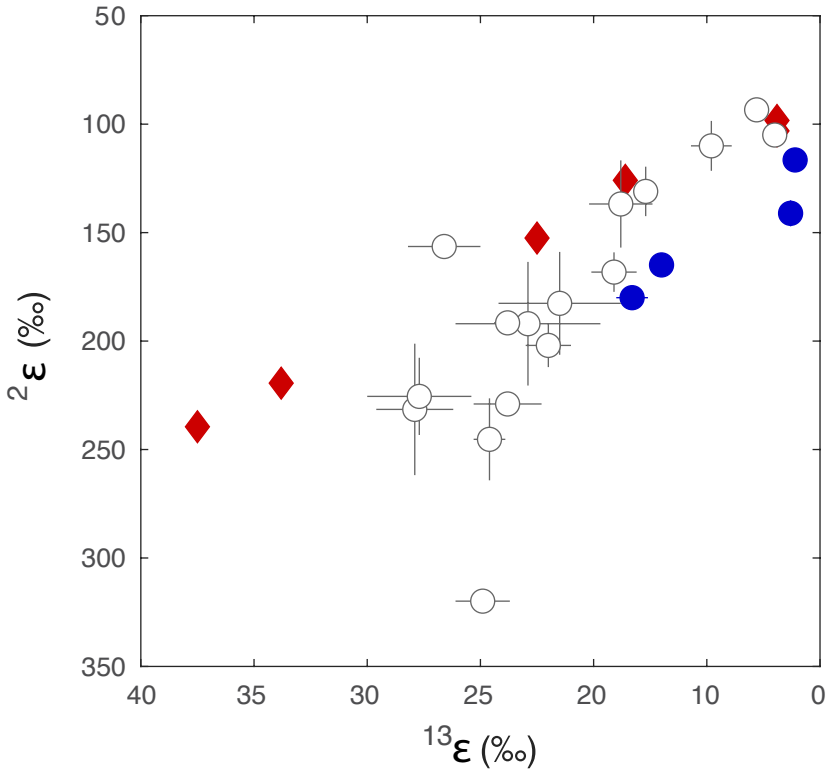

Fig. 2: Carbon and hydrogen isotope fractionations for aerobic and anaerobic microbial methane oxidation during laboratory culture experiments. Anaerobic oxidation of methane from this study and in psychrophilic AOM cultures from Holler et al. (2009) are shown in filled symbols (blue circles and red diamonds, respectively). They are compared with data for aerobic oxidation of methane shown in open symbols (data from Coleman et al., 1981, Kinnaman et al., 2007; Powelson et al., 2007; Wang et al., 2016).

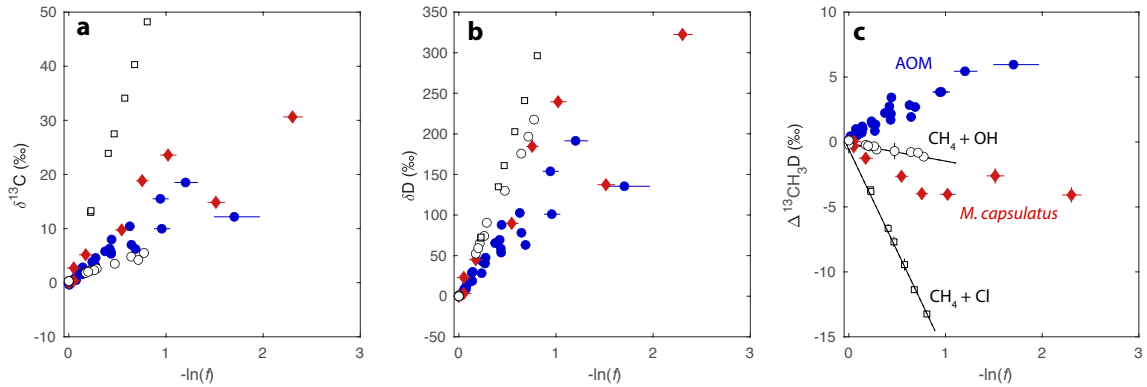

Fig. 3: Evolution of (a) $\delta^{13}C$, (b) δD and (c) $\Delta^{13}CH_3D$ values of residual methane during different methane oxidation processes. Methane oxidation by AOM (this study, filled blue circles), aerobic methane oxidation by *M. capsulatus* (Wang et al., 2016, filled red diamonds), and gas phase oxidation by OH and Cl radicals (Whitehill et al., 2017, open circles and squares, respectively) are shown. The values for $\delta^{13}C$, δD and $\Delta^{13}CH_3D$ are referenced against initial methane.

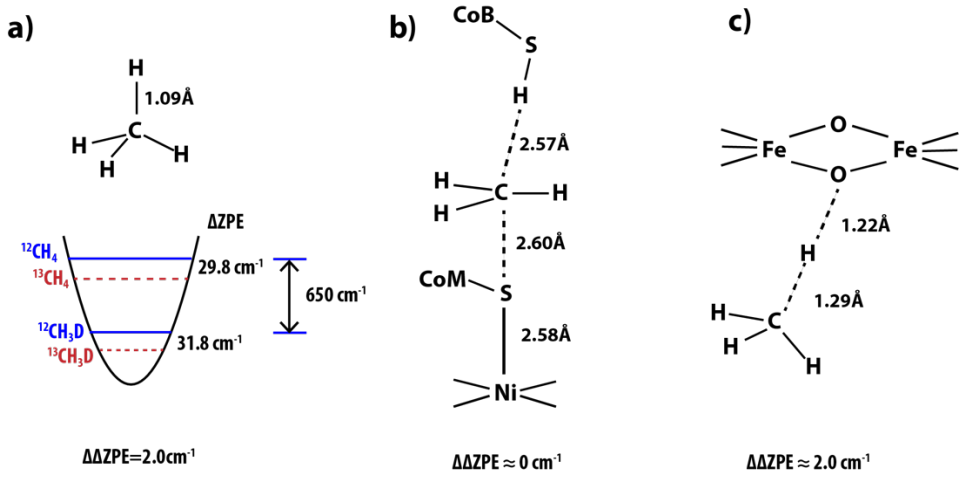

Fig. 4: Illustration of ΔΔZPE effect as the origin of the clumped isotopologue effect. (a) shows that ΔΔZPE of 2 cm^{-1} is the difference in ΔZPE values between $^{13}CH_4/^{12}CH_4$ and $^{13}CH_3D/^{12}CH_3D$. The diagram (b) and (c) show the geometry of transition states around methane activation sites for methyl-S-CoM reductase for AOM (from Wongnate et al., 2016) and sMMO for aerobic methane oxidation (from Huang et al., 2013). Due to the elongated C–H bonds for methyl-S-CoM transition state, the ΔΔZPE effect is expected to be much smaller than 2 cm^{-1} at the transition state.

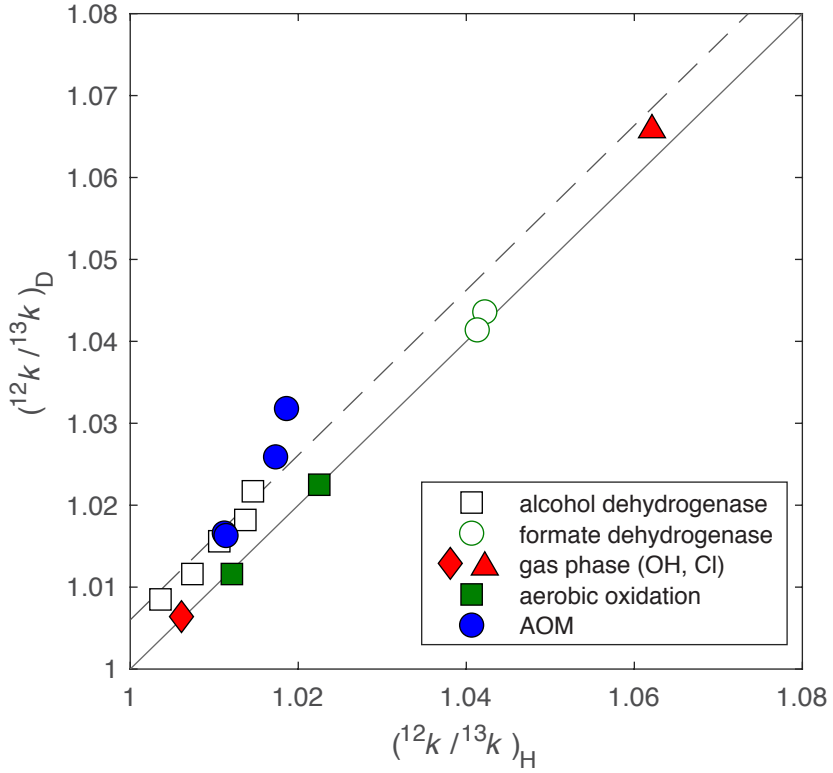

Fig. 5: Double isotope effect for C-H bond breaking reactions. Here, carbon kinetic isotope effect (k_{12}/k_{13}) is compared for non-deuterated versus deuterated compounds. Filled circles, AOM (this study); filled squares, aerobic methane oxidation (Wang et al., 2018); filled triangle and diamond, oxidation by OH and Cl radicals (Whitehill et al., 2017); open square, alcohol dehydrogenase (Scharschmidt et al., 1984); and open circle, formate dehydrogenase (Hermes et al., 1984). The solid line shows 1:1 relationship, which is expected when there is no intrinsic clumped effect. Dashed line shows 1:1.006 relationship, which is expected for clumped isotope effect of 6‰.

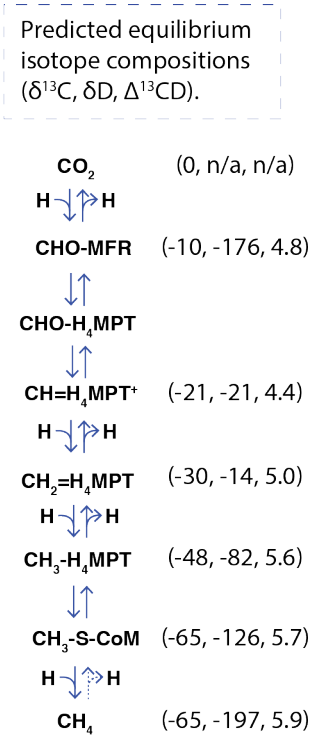

Fig. 6: A schematic showing the pathway of hydrogenotrophic methanogenesis and approximate equilibrium isotope and isotopologue fractionations estimated from truncated molecular simulation (Wang et al., 2015). Predicted isotope compositions, $\delta^{13}C$ and δD (in ‰), are referenced to those of CO_2 and H_2O, respectively, and $\Delta^{13}CD$ value is against stochastic distributions. Pathway is taken from Thauer (2011). Abbreviations are: MFR, methanofuran; H_4MPT, tetrahydromethanopterin; CoM, coenzyme M. The last reaction, reduction of methyl-S-CoM to methane is exergonic and often unidirectional, and is hypothesized to be the source of kinetic D- and $^{13}CH_3D$-isotope signals of microbial methane.

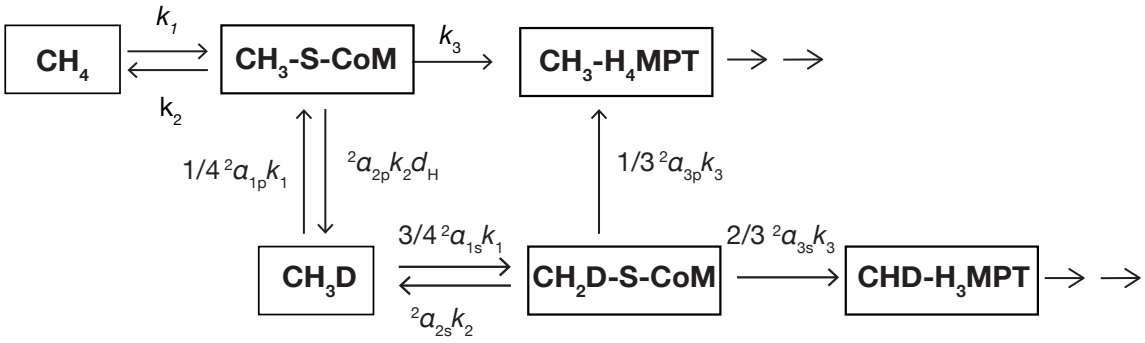

Figure A1: The reaction scheme used to derive the modified Rayleigh equation that includes the reversibility of the first step. See text for symbols.

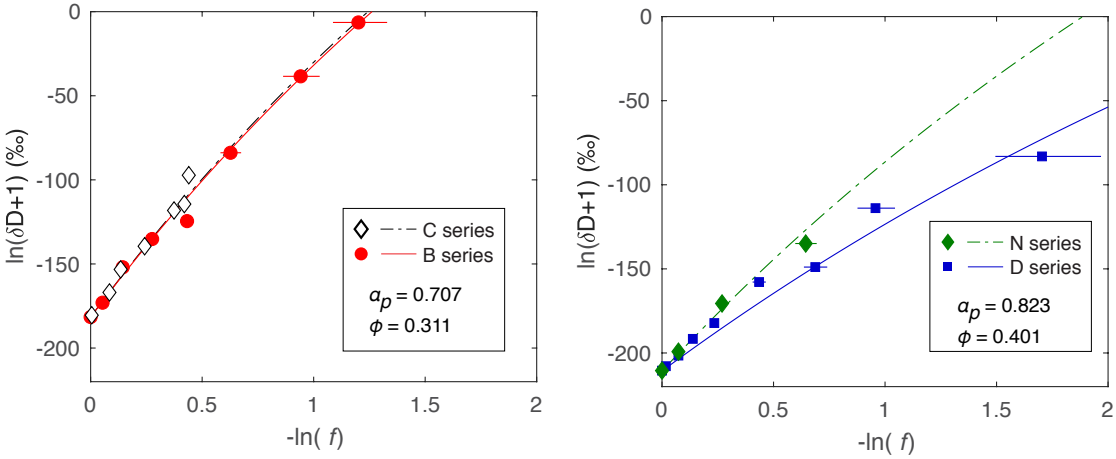

Figure A2. Model fit to the data for four experiments. The best fit was obtained for primary D/H fractionation factor (α_{1p}) of 0.707 and forward commitment (ϕ) of 0.311 for B- and C-series experiments, and 0.823 and 0.401, respectively for D and N series experiments.